Pure Appl. Geophys.

DOI 10.1007/s00024-017-1567-1

Pure and Applied Geophysics

Reduction of Injection-Induced Pore-Pressure and Stress in Basement Rocks Due to Basal Sealing Layers

Kyung Won Chang[1,2] and Paul Segall[1]

Abstract—Our previous study (Chang and Segall, J Geophys Res Solid Earth 121(4):2708–2726, 2016a) demonstrated that diffusion of pore-pressure and stress into basement rocks can cause slip on deep faults, potentially inducing seismicity. Recent studies suggest that the presence of a bottom-sealing layer between the injection horizon and basement will reduce the magnitude of injection-induced pore-pressure in the basement due to contrasts in permeability and/or storage capacity. In this study, we examine the role of basal sealing horizons in induced seismicity on basement faults by adding a layer beneath the reservoir into the two-dimensional, fully coupled poroelastic model developed previously. We consider two types of basal seals: (1) a low-permeability seal and (2) a high-storativity seal. The analysis of the spatio-temporal change in Coulomb stress and time-dependent rate of earthquake nucleation confirms that both types of seal inhibit direct pore-pressure diffusion into basement rocks, but poroelastic stresses are still transmitted, potentially inducing earthquakes. The high-storativity seal reduces the transmission of poroelastic stresses into the basement, minimizing seismicity on basement faults in comparison to the low-permeability seal.

Key words: Induced seismicity, basement faults, bottom seal, poroelastic stressing.

1. Introduction

The success of fluid injection projects, i.e. wastewater disposal and geological carbon dioxide (CO_2) storage, hinges on how much fluid can be stored in the subsurface without inducing instabilities in the geological formations. Increased pore-pressures can lead to geological risks including (1) upward migration of injected fluids or in situ brine through faults or fractures, and (2) induced earthquakes, particularly in basement formations which may host larger faults. In addition to diffusion of pore-pressure, fluid injection deforms the reservoir and bounding formations, and excessive deformation can reactivate pre-existing faults and fractures.

Leakage of injected fluids into an overlying groundwater system can have deleterious impacts on the quality of potable water (Little and Jackson 2010; Siirila et al. 2012). An intact confining seal, consisting of shale, siltstone, or other fine-grained clastic rock, is essential to secure injected fluids within the target reservoir, and its hydraulic properties and thickness control the rate of fluid leakage through the seal (Tofflemire and Brezner 1971; Hou et al. 2012; Song and Zhang 2013). At the same time pore-pressure dissipation into bounding formations attenuates the lateral propagation of the pressure plume within the target reservoir. This may enhance the amount of fluid that can be safely injected into the formation before exceeding a specified pressure limit (Birkholzer et al. 2009; Chang et al. 2013).

In some cases wastewater disposal into deep formations can lead to induced earthquakes, some large enough to be damaging. The majority of induced earthquakes of significant magnitude occurred within basement rocks (Horton 2012; Kim 2013; Kerenan et al. 2013; Frohlich et al. 2014). Previous modeling studies assume no sealing layer below the target reservoir, which allows direct diffusion of pore-pressure into basement rocks (Zhang et al. 2013; Kerenan et al. 2014). Few studies also consider indirect transfer of poroelastic stresses to basement faults, which occurs without direct pore-pressure diffusion to depth, and also has the potential for inducing seismicity (Ellsworth 2013; Segall and Lu

[1] Department of Geophysics, Stanford University, Stanford, CA 94305, USA. E-mail: kchang@sandia.gov; segall@stanford.edu
[2] *Present Address*: Geomechanics Department, Sandia National Laboratories, Albuquerque, NM 87185, USA.

Published online: 17 May 2017

2015). Recently, Chang and Segall (2016a) tested different types of basement faults with variations in hydraulic connectivity to the reservoir as well as permeability and showed that earthquakes can be triggered by both pore-pressure diffusion or injection-induced poroelastic stressing, depending on the stress regime and properties of faults and basement rock. Chang and Segall (2016b) further examined the feasibility of simultaneous fluid extraction to mitigate the potential of injection-induced seismicity on basement faults. They concluded that fluid extraction significantly reduces pore-pressure buildup, but that production-induced poroelastic stressing can trigger earthquakes depending on fault geometry, injection/extraction parameters, background stressing rate, and friction parameters.

Recent studies note that a seal below the storage formation limits pore-pressure diffusion into the basement and may thus prevent deep injection-induced earthquakes (Vilarrasa and Carrera 2015; Walsh and Zoback 2015). Downward diffusion of elevated pore-pressure into the basement can potentially triggering earthquakes on critically stressed faults. Based on the above findings, we investigate how effectively a bottom-sealing layer diminishes injection-induced seismicity on basement faults by modeling both pore-pressure diffusion and poroelastic interaction between the formation, sealing layers, and bounding sequences. In particular, we study how varying the permeability and storativity (compressibility) of the sealing layer influences pore-pressure and stress diffusion.

Vertical diffusion between layers depends on the vertical permeability and storativity of the seals. The effective permeability of sealing formations ranges from 10^{-23} to 10^{-17} m^2 based on laboratory studies (Neuzil 1994), but in-situ sealing units may exhibit higher permeability due to the presence of interbedding of coarser sediments and/or small-scale fractures. Previous laboratory measurements (summarized in Rieke and Chilingarian 1974) determine rock (bulk) compressibility as a function of pressure which shows that clay-rich mudrocks have compressibilities up to 2 orders of magnitude higher than fluids at depths of up to 3 km and 1–3 orders of magnitude higher than reservoir rocks, which range from 10^{-11} to 10^{-9} Pa^{-1} at depths greater than 1 km (Ge and Garven 1992). This suggests that the characteristic diffusive length x_c ranges from 10^{-4} to 1 km, where $x_c = \sqrt{4c_{sl}\Delta t}$ defined by the hydraulic diffusivity of the seal $c_{sl} = \kappa_{sl}/\eta S_{sl}$, in which κ (m^2) is permeability, η (Pa s) is the fluid viscosity, and S (Pa^{-1}) is storativity, and injection period $\Delta t = 1$ year, such that fluid injection sites span the range of almost no diffusion to a considerable diffusion into sealing formations.

Including poroelastic coupling in the analysis reveals that gradients in pore-pressure act as body forces in the stress equilibrium equations, thus inducing deformation of the porous rock (fluid-to-solid coupling), while conversely a change in volumetric strain perturbs the pore-pressure field (solid-to-fluid coupling) (Biot 1941; Rice and Cleary 1976; Wang 2000; Segall 2010). These effects are not accounted for considering only uncoupled pore-pressure diffusion. The magnitude of the fluid-to-solid coupling depends on the Biot–Willis coefficient α relating changes in pore-pressure to volumetric strain, Eq. (1) below. The magnitude of the solid-to-fluid coupling depends on storativity which is a function of poroelastic coefficients, i.e. Biot–Willis coefficient α or Skempton's coefficient B [Eq. (8) in Sect. 2]. Note that negligible solid-to-fluid coupling occurs for a highly compressible fluid, e.g. gas. The variation in permeability and storativity of different formations can affect rock deformation as well as fluid flow through deformable pores, and thus, the formation may undergo a range of possible poroelastic responses to fluid injection.

In this study, a four-layer system is modeled including high-permeability (conductive) basement faults hydraulically isolated from the target reservoir. Two types of bottom seals are investigated: (1) a low-permeability seal and (2) a high-storativity seal. We perform numerical calculations including full poroelastic coupling and time-dependent earthquake nucleation to examine the effect of bottom-sealing layers on seismicity on basement faults. In Sect. 2 we describe the governing equations of poroelasticity in two-dimensional plane strain. In Sect. 3.1 we quantify the amount of fluids displaced into bounding sequences relative to the target formation. In Sect. 3.2 we examine the attenuation of Coulomb stress changes through the bottom seal. In Sect. 3.3

we compute the seismicity rate on basement faults for different types of bottom seals. We quantify the effect of physical properties of the bottom-sealing layer on the stability of basement faults and emphasize the importance of reservoir characterization prior to fluid injection operations.

2. Model Formulation

As in our previous studies (Chang and Segall 2016a, b), we use the equations for an isotropic, fluid-saturated poroelastic medium. The following linear constitutive equations describe strain of the rock ϵ_{ij} and alteration in pore-fluid mass Δm as a function of stress σ_{ij} and pore-pressure p (Biot 1941; Rice and Cleary 1976; Wang 2000; Segall 2010):

$$2G\epsilon_{ij} = \sigma_{ij} - \frac{\nu}{1+\nu}\sigma_{kk}\delta_{ij} + \frac{(1-2\nu)\alpha}{1+\nu}p\delta_{ij}, \tag{1}$$

$$\Delta m = \frac{9\rho_{\mathrm{f}}(\nu_{\mathrm{u}}-\nu)}{2GB2(1+\nu)(1+\nu_{\mathrm{u}})}\left(\frac{B\sigma_{kk}}{3}+p\right), \tag{2}$$

where G (Pa) is the shear modulus, ν (−, dimensionless) and ν_{u} are the Poisson's ratio for drained and undrained conditions, and α (−) is Biot–Willis coefficient. Δm (kg/m^3) is the increment in fluid mass per unit rock volume, as measured in the undeformed state. ρ_{f} (kg/m^3) is the fluid density and B (−) is Skempton's coefficient giving the ratio of the change in pore-pressure to the change in mean normal stress under undrained ($\Delta m = 0$) conditions, $p = -B\sigma_{kk}/3$. Note that only two of the parameters B, α, and ν_{u} are independent. The fluid mass change can be expressed in terms of the compressibility, which is one of the major parameters varied in this study, from Eq. (2)

$$\Delta m = \frac{\rho_{\mathrm{f}}\alpha}{KB}\left(\frac{B}{3}\sigma_{kk}+p\right), \tag{3}$$

where $1/K$ (Pa^{-1}) is the drained rock bulk compressibility which is the volumetric strain $\epsilon \equiv \epsilon_{kk}$ due to changes in applied stress while holding pore-pressure constant, expressed in terms of G and ν (Wang 2000)

$$\frac{1}{K} = \left.\frac{\delta\epsilon}{\delta\sigma}\right|_{p=0} = \frac{3(1-2\nu)}{2G(1+\nu)}. \tag{4}$$

Combining the first constitutive Eq. (1) with the local stress balance equation

$$\sigma_{ij,j} = -\mathbf{f}_i, \tag{5}$$

where $\mathbf{f}_i = \rho g_i$ is the component of the body force per unit volume of the bulk material, $\rho = (1-\phi)\rho_{\mathrm{s}} + \phi\rho_{\mathrm{f}}$ is the bulk density (ρ_{s} is solid density and ϕ is porosity) and g_i (m/s^2) is the component of gravitational acceleration, and yields quasi-static equilibrium equations in terms of displacement u_i and pore-pressure p (e.g. Segall 2010, Chapter 10)

$$\nabla\cdot[G(\mathbf{x})\nabla\mathbf{u}] + \nabla\left[\frac{G(\mathbf{x})}{1-2\nu(\mathbf{x})}\right]\nabla\cdot\mathbf{u} - \alpha(\mathbf{x})\nabla p + \mathbf{f} = 0. \tag{6}$$

In Eq. (6), pore-pressure gradients act in the same way as body forces $\mathbf{f}$, and induce deformation of the solid. Substituting the second constitutive Eq. (2) into the continuity equation for fluid mass

$$\frac{\partial m}{\partial t} + \nabla\cdot\mathbf{q} = 0, \tag{7}$$

where $\mathbf{q}$ (kg/s) is fluid mass flux and Darcy's law $\mathbf{q} = -(\rho_{\mathrm{f}}\kappa/\eta)\nabla p$ is employed, gives the flow equation for single-phase transient flow in a heterogeneous and isotropic compressible porous medium. This can be written in the form of an inhomogeneous diffusion equation for pore-pressure p (Wang 2000; Segall 2010):

$$S(\mathbf{x})\frac{\partial p}{\partial t} - \frac{1}{\eta}\nabla\cdot[\kappa(\mathbf{x})\nabla p] = -\alpha(\mathbf{x})\frac{\partial}{\partial t}(\nabla\cdot\mathbf{u}) + Q(\mathbf{x},t), \tag{8}$$

where Q is volume of fluid added from an external source (per unit bulk volume per unit time) and S (Pa^{-1}) is the constrained specific storage (Wang 2000), representing the fluid volume change (per unit control volume) due to pressure change while holding the control volume constant, given in terms of other poroelastic constants by

$$S = \frac{\alpha^2(1-2\nu)(1-2\nu_{\mathrm{u}})}{2G(\nu_{\mathrm{u}}-\nu)}. \tag{9}$$

Note that full poroelastic coupling is defined by the presence of ∇p in Eq. (6) and $\nabla\cdot\mathbf{u}$ in the flow equation (8).

Including an additional layer for the basal seal, relative to our previous studies, we consider a four-layer geometry comprising a laterally extensive sandstone reservoir ($L = 40$ km; $H_s = 0.1$ km) overlain by a thick mudrock sequence ($H_m = 0.5$ km) and underlain by a sealing layer ($H_{sl} = 0.25$ km) and basement rock ($H_b = 2.75$ km) as shown in Fig. 1. The two-dimensional ($\mathbf{x} = (x_1, x_3)$) plane strain ($\partial(\cdot)/\partial x_2 = 0$) domain has origin at the middle of the sandstone reservoir bottom (depth of 3 km). The spatial variation of the physical properties in this layered geometry is given by

$$\kappa(\mathbf{x}) = \begin{cases} \kappa_m; & x_3 > H_s \\ \kappa_s; & 0 \le x_3 \le H_s \\ \kappa_{sl}; & -H_{sl} \le x_3 \le 0 \\ \kappa_b; & x_3 < -H_{sl} \end{cases}, \tag{10}$$

$$S(\mathbf{x}) = \begin{cases} S_m; & x_3 > H_s \\ S_s; & 0 \le x_3 \le H_s \\ S_{sl}; & -H_{sl} \le x_3 \le 0 \\ S_b; & x_3 < -H_{sl} \end{cases}, \tag{11}$$

where the subscripts m, s, sl, and b represent mudrock, sandstone, seal, and basement rock. To investigate the effect of the bottom-sealing sequence on the perturbation in pore-pressure and stress fields, we model two end-member types of seals: a low-permeability seal and a high-storativity seal. For the low-permeability seal, we choose $\kappa_{sl} = 1 \times 10^{-19}$ m^2, an intermediate value relative to previous modeling studies of geologically layered system (refer to Table 2 in Chang et al. 2013), which gives $\kappa_{sl}/\kappa_b = 5 \times 10^{-3}$ and $\kappa_{sl}/\kappa_s = 1.5 \times 10^{-6}$. For the high-storativity seal, we choose $G_{sl} = 2$ GPa ($1/K_{sl} = 3.7 \times 10^{-10}$ Pa^{-1}; 3 times more compressible than the sandstone reservoir), based on laboratory measurement of mechanical properties of shale (Islam and Skalle 2013), which results in $S_{sl}/S_b = 50$ and $S_{sl}/S_s = 4$ in this study. For simplicity we assume that other parameters remain the same as values used for basement rocks. Note that storativity S depends on parameters other than shear modulus, for example $\nu_u - \nu$ [refer to Eq. (9)], which will be discussed in Sect. 3.2; however, to isolate the effect of changes in storativity, we change only the shear modulus here. A three-layer system without a bottom-sealing layer is modeled as a reference case. Hydrological and mechanical properties of each layer are given in Table 1.

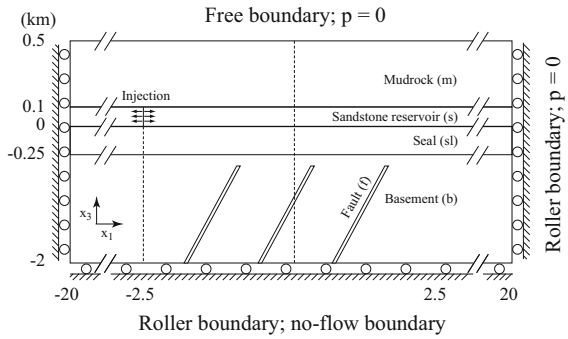

Figure 1
Schematic description of the numerical model with boundary conditions. Laterally extensive geometry ($L_w \gg x_c = \sqrt{4c_s\Delta t}$, where L_w is the distance from the injection well to the outer boundary and x_c is characteristic length for pressure diffusion) minimizes boundary effects on pore-pressure. Basement faults are assumed conductive and well-oriented to slip in a normal faulting stress state

As we are concerned with perturbations from an initial self-equilibrated stress state, we set the initial stresses and pore-pressure to zero. Fluids are uniformly injected along the reservoir thickness ($H_s = 100$ m) at constant mass rate of 0.3 kg/m s for $\Delta t = 30$ days, but the numerical simulation runs for 300 days in order to investigate post shut-in behavior. Hydraulically, the top and side boundaries have constant pressure condition $p = 0$ while the bottom boundary has a no-flow condition representing underlying impermeable sequences. Mechanically, the top boundary is traction free, while the side and bottom boundaries are free to move in the surface-parallel direction. A laterally and vertically extensive geometry allows us to neglect boundary effects associated with diffusion ($L_w = 17.5$ km $\sim 6x_{c,1}$ and $H_b = 3$ km $\sim 15x_{c,3}$, where subscripts 1 and 3 represent horizontal and vertical coordinates, and $x_c = \sqrt{4c_{sl}\Delta t}$ as defined previously). The basement contains a set of 60° dipping normal faults, as in Chang and Segall (2016a). We assume that faults are well-oriented for slip in the ambient stress state.

First, we estimate how much fluid is displaced into each sequence for different types of bottom seals, using the injection-induced perturbation in pore-pressure and stresses. This quantifies the effect of the seals on diffusion of pore-pressure as well as

Table 1

Summary of model properties

Model properties	Mudrock[a]	Sandstone[a]	Seal[b]	Basement[b]	Fault[b]	Fluid
κ^c (m^2)	1×10^{-19}	6.4×10^{-14}	1×10^{-19}	2×10^{-17}	1×10^{-13}	–
ϕ (−)	0.1	0.25	0.1	0.05	0.02	–
G (GPa)	11.5	7.6	2	25	6	–
ν (−)	0.3	0.15	0.2	0.2	0.2	–
ν_u (−)	0.35	0.25	0.31	0.25	0.33	–
B (−)	0.8	0.62	0.55	0.85	0.62	–
f (−)	0.5	0.6	0.5	0.6	0.75	–
C (MPa)	75	80	75	130	0	–
ρ (kg/m^3)	2600	2500	2600	2740	2500	1000
η (Pa s)	–	–	–	–	–	1×10^{-3}

[a] Mudrock and sandstone properties are based on Kim and Hosseini (2013)

[b] Seal properties are modified for the sensitivity tests: (1) low-permeability ($\kappa_{sl}/\kappa_b = 0.005$; $S_{sl}/S_b = 1$) and (2) high-storativity seal ($\kappa_{sl}/\kappa_b = 1$; $S_{sl}/S_b = 50$)

[c] Hydrological properties of basement and faults are based on tabulation in Zhang et al. (2013), and mechanical properties are based on Stanislavsky and Garven (2002) and Willson et al. (2007)

transmission of stress into the basement. Then, we compute normal and shear stresses, σ_n and τ_s, on the basement faults and obtain the spatiotemporal distribution of Coulomb stress $\tau = \tau_s + f(\sigma_n + p) = \tau_s + f\bar{\sigma}$, where f is fault friction coefficient (assumed constant) and $\bar{\sigma}$ is effective normal stress. This allows us to investigate the effects of basal seals on the poroelastic response of the basement faults. We assume the ratio of shear stress to effective normal stress, $\tau_s/\bar{\sigma}$, is relatively constant with only small changes, and follow Segall and Lu (2015) to obtain the seismicity rate using the Dieterich (1994) formulation as follows:

$$\frac{dR}{dt} = \frac{R}{t_a}\left(\frac{\dot{\tau}}{\dot{\tau_0}} - R\right), \tag{12}$$

where R is the seismicity rate relative to an assumed prior steady-state seismicity rate at a background stressing rate $\dot{\tau}_0$, and $t_a \equiv A\bar{\sigma}/\dot{\tau}_0$ is the characteristic aftershock decay time. In this study, we assume the constitutive parameter $A = 0.005$ quantifying the "direct effect" in the rate-state friction law, and the effective normal stress acting on the fault plane $\bar{\sigma} =$ 10 MPa at a depth of about 1 km. The background stressing rate $\dot{\tau}_0$ is assumed to be 10^{-3} MPa/years, such that a typical 1 MP stress drop accumulates in 10^3 years. This leads to a characteristic time of $t_a =$ 50 years. We solve the ordinary differential Eq. (12) to obtain $R(\mathbf{x}, t)$ along the basement faults near the injector using the Matlab ODE solver `ode45`. The details of the numerical procedure can be found in Chang and Segall (2016a).

3. Numerical Results

We perform finite-element simulations governed by Eqs. (6) and (8), employing the parameter fields (10) and (11), and initial and boundary conditions to study the perturbation in pore-pressure and stresses driven by fluid injection. The finite-element analysis is conducted using COMSOL Multiphysics (2014) using bilinear quadrilateral elements for spatial discretization (Hughes 2000) and a variable step method for time integration (Dreij et al. 2011). We adapt a highly refined mesh near the boundaries between layers as well as the basement faults to resolve the strong pressure gradients typical of these problems.

3.1. Displacement of Fluids Into Surrounding Formations

Previous studies of induced seismicity suggest that the total volume of injected fluids may control the rate and maximum magnitude of induced earthquakes (Shapiro et al. 2010; McGarr 2014); however, these arguments generally neglect the effect of heterogeneous properties on local perturbations in

pore-pressure and stress, especially near critically stressed faults. The volume of displaced fluids into the target reservoir as well as the bounding sequences will vary corresponding to their hydrological and mechanical properties. If the maximum magnitude of an earthquake confined to the basement scales with the volume of fluids displaced into basement rocks, it will be useful to quantify this effect. In a poroelastic system, the increase in fluid mass affects both pore-pressure and stress fields, and thus ultimately the Coulomb stress change.

Before looking into the Coulomb stress perturbation, we quantify how the presence of a sealing layer beneath the reservoir affects the mass of displaced fluids into the basement. In a geologically layered formation, the fluid mass displaced into each sequence is determined by formation properties, i.e. permeability and storativity. Given Eq. (2) for the change in fluid mass, we calculate the amount of the fluid stored in each layer using the following equations:

$$\begin{cases} m_{\mathrm{m}} = \int_{H_{\mathrm{s}}}^{+\infty}\int_{-\infty}^{+\infty} \Delta m \, \mathrm{d}x_1 \mathrm{d}x_3, \\ m_{\mathrm{s}} = \int_{0}^{H_{\mathrm{s}}}\int_{-\infty}^{+\infty} \Delta m \, \mathrm{d}x_1 \mathrm{d}x_3, \\ m_{\mathrm{sl}} = \int_{-H_{\mathrm{sl}}}^{0}\int_{-\infty}^{+\infty} \Delta m \, \mathrm{d}x_1 \mathrm{d}x_3, \\ m_{\mathrm{b}} = \int_{-\infty}^{-H_{\mathrm{sl}}}\int_{-\infty}^{+\infty} \Delta m \, \mathrm{d}x_1 \mathrm{d}x_3, \end{cases} \tag{13}$$

where m_i (kg) is the mass of displaced fluids in each sequence, and the fraction of the total injected mass stored in each sequence is quantified by the ratio of fluid mass f_i as follows:

$$f_i = \frac{m_i}{\sum_{i=\mathrm{m,s,sl,b}} m_i}. \tag{14}$$

Figure 2 shows the temporal evolution of m_i and f_i for two types of bottom-sealing layers: (1) low-permeability seal (blue line) and (2) high-storativity seal (red line). The reference case (no-seal) is shown as a gray line. The dashed line represents the end of injection at $\Delta t = 30$ days.

The low-permeability seal hinders vertical diffusion into the basement rocks (blue line in Fig. 2a), which confines fluids within the target reservoir (Fig. 2b) with slightly more diffusion into overlying mudrock (Fig. 2c) compared to the reference case. Note that low-permeability mudrock sequence does not absorb significant fluid mass ($m_{\mathrm{m}}/m_{\mathrm{s}} < 0.07$). On the other hand, the high-storativity (high-compressibility) seal allows six times more fluids into the bottom sequences relative to the reference case (red line in Fig. 2a). The high-storativity seal acts as a "cushion" absorbing fluids, instead of limiting diffusion. Assuming the same injected volume, the large fluid loss into the compressible seal

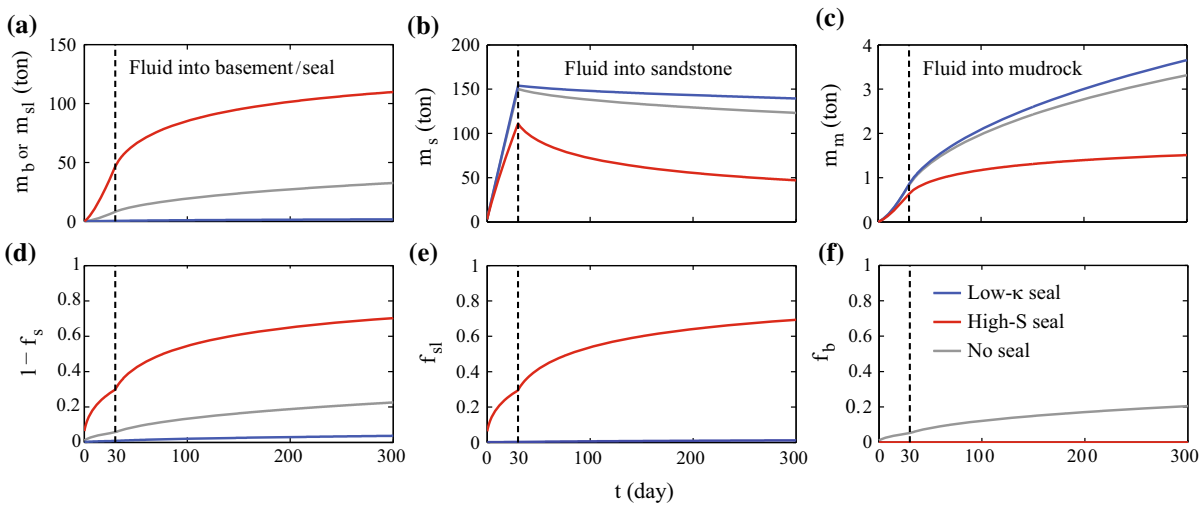

Figure 2
Comparison of fluid mass displaced into each sequence m_i and mass fraction f_i (i = m, s, sl, and b). The cases including a bottom sealing layer with low permeability ($\kappa_{\mathrm{sl}}/\kappa_{\mathrm{b}} = 0.005$; *blue line*) or high compressibility ($S_{\mathrm{sl}}/S_{\mathrm{b}} = 50$; *red line*) are compared to the case of no sealing layer between a sandstone layer and the basement (*gray line*)

reduces fluid mass diffusion into the reservoir and overlying mudrock (Fig. 2b, c). Figure 2d shows the mass fraction of fluids stored in the bounding sequences for the three cases, which increases with time because fluids continue to dissipate into permeable and compressible sequences after shut-in. However, the physics of fluid displacement/storage varies depending on the type of the bottom seal (Fig. 2e, f). The low-permeability seal inhibits vertical diffusion across the seal, and no fluids are stored in the basement (fluids are confined within the sandstone reservoir). On the contrary, the high-storativity seal absorbs fluids, such that only a tiny amount of fluid invades the basement.

These results show that a bottom-sealing layer with low permeability and high storativity will be the most effective in limiting fluid diffusion into deep basement rocks. However, the estimate of the displaced fluid mass (13) does not capture local perturbations in pore-pressure and stresses acting on basement faults at depth driven by poroelastic coupling. To quantify the effect of the bottom seal on fault stability, we compute the spatiotemporal distribution of pore-pressure and stress to investigate how bottom-seals effect the Coulomb stress change acting on basement faults. In addition to direct pore-pressure buildup, poroelastic stresses due to fluid injection may limit well operations in order to avoid induced seismicity on basement faults.

3.2. *Coulomb Stress Change*

As discussed in Sect. 3.1, the bottom-sealing layer reduces direct diffusion of pore-pressure into the basement. Poroelastic stresses, however, are transmitted and can affect the stability of basement faults (Chang and Segall 2016a, b). Elevated pore-pressure within the reservoir causes it to expand, inducing horizontal extension of the underlying sequences below the region experiencing significant pore-pressure increase. More distal regions are subjected to horizontal compression. Without direct pore-pressure diffusion, poroelastic deformation thus can potentially induce slip on basement faults at depth, depending on the orientation and location of basement faults, the pre-existing state of stress, and the properties of the underlying sequences (Chang and Segall 2016a). Vertical heterogeneity in these sequences determines the extent of downward pore-pressure diffusion as well as poroelastic stressing of the formations. In this study, we focus on how the presence of the bottom-sealing layer affects mechanical stability of critically stressed faults in the basement including poroelastic stressing.

To investigate the poroelastic response to fluid injection, we compute the change in Coulomb stress acting on pre-existing fault planes, assuming a friction coefficient f, in terms of the changes in poroelastic stresses and pore-pressure

$$\Delta\tau = (\Delta\tau_s + f\Delta\sigma_n) + f\Delta p, \tag{15}$$

where $\Delta\tau$ is the change of Coulomb failure stress, $\Delta\tau_s$ is the change in shear stress, $\Delta\sigma_n$ is the change in normal stress, Δp is the change in pore-pressure. Positive values of $\Delta\tau$ imply that the fault plane is moved closer to failure; positive values of $\Delta\tau_s$ indicate that the change in shear stress favors failure in the expected slip direction of the fault (here taken to be normal slip); positive values of $\Delta\sigma_n$ imply an increase in relative tension across the fault.

Figure 3a–c (top row) shows the change in the poroelastic stresses, $\Delta\tau_s + f\Delta\sigma_n$, at $t = 200$ days for three cases. For the reference case with no bottom seal, a positive poroelastic stress change is observed in the basement well below the target reservoir due to injection-induced dilation of the reservoir. This leads to increases in both $\Delta\sigma_n$ and $\Delta\tau_s$ (Fig. 3a). Within the zone of elevated pore-pressure, a negative change in poroelastic stress partially compensates for the increase in pore-pressure. In the case of a low-permeability underlying seal, the limited pore-pressure diffusion reduces the zone of negative poroelastic stress, however a positive poroelastic stress change develops in both the seal and basement (Fig. 3b). In the case of a high-storativity underlying seal, almost no changes are observed within the seal, and a modest increase in poroelastic stresses is observed in the basement (Fig. 3c).

The smaller magnitude of $\Delta\tau_s + f\Delta\sigma_n$ within the basement in the low-permeability case can be understood as follows: the low-permeability seal causes the pore-pressure change within the storage formation to spread out more laterally. This decreases the horizontal pressure gradient, thereby reducing the stresses

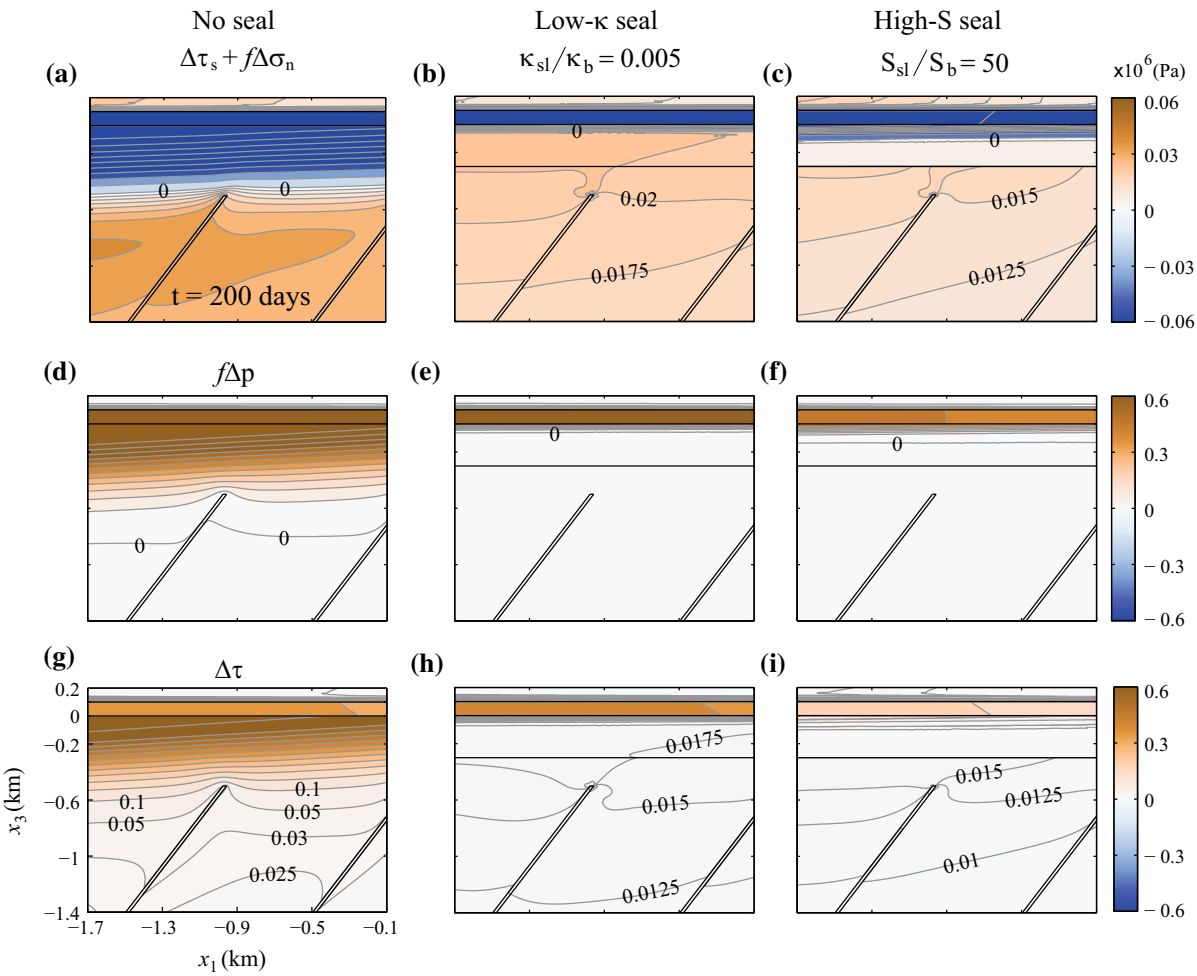

Figure 3
Changes in poroelastic stresses $\Delta\tau_s(\mathbf{x}) + f\Delta\sigma_n(\mathbf{x})$, pore-pressure $f\Delta p(\mathbf{x})$, and Coulomb stress $\Delta\tau(\mathbf{x})$ at $t = 200$ days for isolated/conductive faults: (1) no seal above basement rocks (*left column*), (2) low-permeability seal (*middle column*), and (3) high-storativity seal (*right column*)

acting on the basement faults. In the other case, the high-storativity seal reduces the pore-pressure perturbation within the seal, even if the same amount of fluid is stored there [refer to the Eqs. (2) and (8)]. Reducing G increases S [refer to Eq. (9)] that decreases the pore-pressure change for a given injection because the rock can "absorb" more fluid mass. The compliant (low G) seal accommodates the poroelastic strain with little stress change, thereby limiting the stress transferred to the basement faults.

Figure 3d–f (middle row) shows the change in the pore-pressure, $f\Delta p$, at $t = 200$ days for the three cases. Without a bottom-sealing layer (reference case), post shut-in diffusion allows a downward expansion of the pressurized zone. Once the pressure plume encounters the conductive faults, flow into the faults causes the local pressure gradients to be directed into the faults, distorting the pore-pressure contours (Fig. 3d). Both types of bottom seals inhibit pore-pressure diffusion directly into the basement (Fig. 3e, f).

Figure 3g–i (bottom row) show the change in Coulomb stress, $\Delta\tau$ obtained by summing the poroelastic and direct pore-pressure terms in (15). The profile of $\Delta\tau$ is similar to that of $f\Delta p$ (refer to Fig. 3d–f), because pore-pressure changes dominate the Coulomb stress change for this geometry. Without a sealing layer, we observe smaller, but positive,

changes in Coulomb stress in the basement rocks (Fig. 3g). Note that most aftershock studies suggest that an increase of even less than 0.1–0.3 MPa is generally sufficient to trigger seismicity (Stein and Lisowski 1983; Oppenheimer et al. 1988; Toda et al. 1998; Anderson and Johnson 1999). Also, it has been suggested that, for example, the Wenchuan earthquake was triggered by small changes in $\Delta\tau$ (of less than 0.05 MPa) due to reservoir impoundment (Ge et al. 2009). Bottom-sealing layers reduce $\Delta\tau$ significantly, which favors mechanical stability of the faults, although positive $\Delta\tau$ may destabilize the basement faults without direct pore-pressure changes (Fig. 3h–i). Note that a longer duration or higher rate of injection, as suggested in most wastewater or CO_2 injection projects, may increase $\Delta\tau$ on deep basement faults.

As mentioned before, an increase in S can be achieved by reducing $\nu_u - \nu$, rather than G, in which case the drained solid constitutive relationship is unchanged. In the following examples only ν_u is modified so that the drained response remains the same. Figure 4 compares the vertical distributions of $\Delta\tau_s + f\Delta\sigma_n$ along a dashed orange line for three cases: (1) low-permeability seal, (2) high-storativity seal with smaller G, and (3) high-storativity seal with smaller ν_u. For the high-storativity seals, reducing G decreases the poroelastic stress more than reducing ν_u

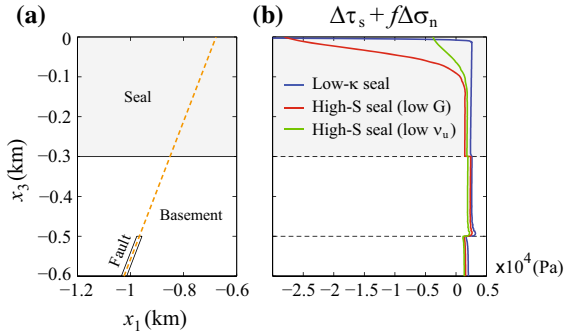

Figure 4
Vertical distribution of poroelastic stress changes $\Delta\tau_s + f\Delta\sigma_n$ along a *dashed orange line*, shown in **a**, at 200 days for three cases: low-permeability seal with smaller κ (*blue*), high-storativity seal with smaller G (*red*), and high-storativity seal with smaller ν_u (*green*). Note that the storativity increases are of the same magnitude ($S_{sl}/S_b = 50$) by reducing either G or ν_u (refer to the Eq. (9))

within the seal, because a smaller G results in the less stress change per unit shear strain.

Figure 5b–d shows the distribution of poroelastic stress, pore-pressure, and Coulomb stress acting parallel to the normal faults along the vertical section at $x_1 = -1.2$ km, indicated as a solid green line in Fig. 5a, for the three cases. The low-permeability seal confines pore-pressure buildup within the target reservoir resulting in the largest changes in $|f\Delta p|$ and $|\Delta\tau_s + f\Delta\sigma_n|$ develop within the reservoir (blue lines). The high-storativity seal absorbs both pore-pressure and stress leading to the smallest changes in $|f\Delta p|$ and $|\Delta\tau_s + f\Delta\sigma_n|$ within the reservoir (red lines). The bottom seals hydraulically isolate the basement, which may minimize fault instability by limiting Coulomb stress changes on basement faults (compared to the reference case with no-seal shown as gray lines).

If conductive faults breach the seal, rapid diffusion into the faults can lead to large increases in Coulomb stress (Chang and Segall 2016a). Figure 5f–g show the distributions of stresses and pore-pressure on the vertical green line in Fig. 5e. The low-permeability seal (blue lines) promotes lateral diffusion of pore-pressure within the reservoir, which could allow enhanced diffusion into more distant, hydraulically connected faults compared to the no-seal case (black lines). In this example, the changes in stress and pore-pressure within the fault zone (located at $x_3 \approx -0.9$ km) are nearly the same for the low-permeability and no-seal cases, although the pore-pressure is slightly higher in the low permeability case. For the high-storativity seal (red lines) pore-pressure perturbations and strains are localized within the seal, such that direct diffusion into the conductive fault is reduced. Thus, the high-storativity seal mitigates the increase in the Coulomb stress change along the faults (Fig. 5h).

To quantify fault stability, we compute the temporal evolution of the net Coulomb stress change $\Delta\tau(t)$ along the basement fault, indicated as a dashed orange line, for three cases shown in Fig. 6a–c. Without a sealing layer (Fig. 6a), the increase in $\Delta\tau$ within the isolated/conductive fault zone occurs due to: (1) poroelastic extension due to dilation of the reservoir, and (2) post shut-in diffusion of pore-pressure (Chang and Segall 2016a). Both types of

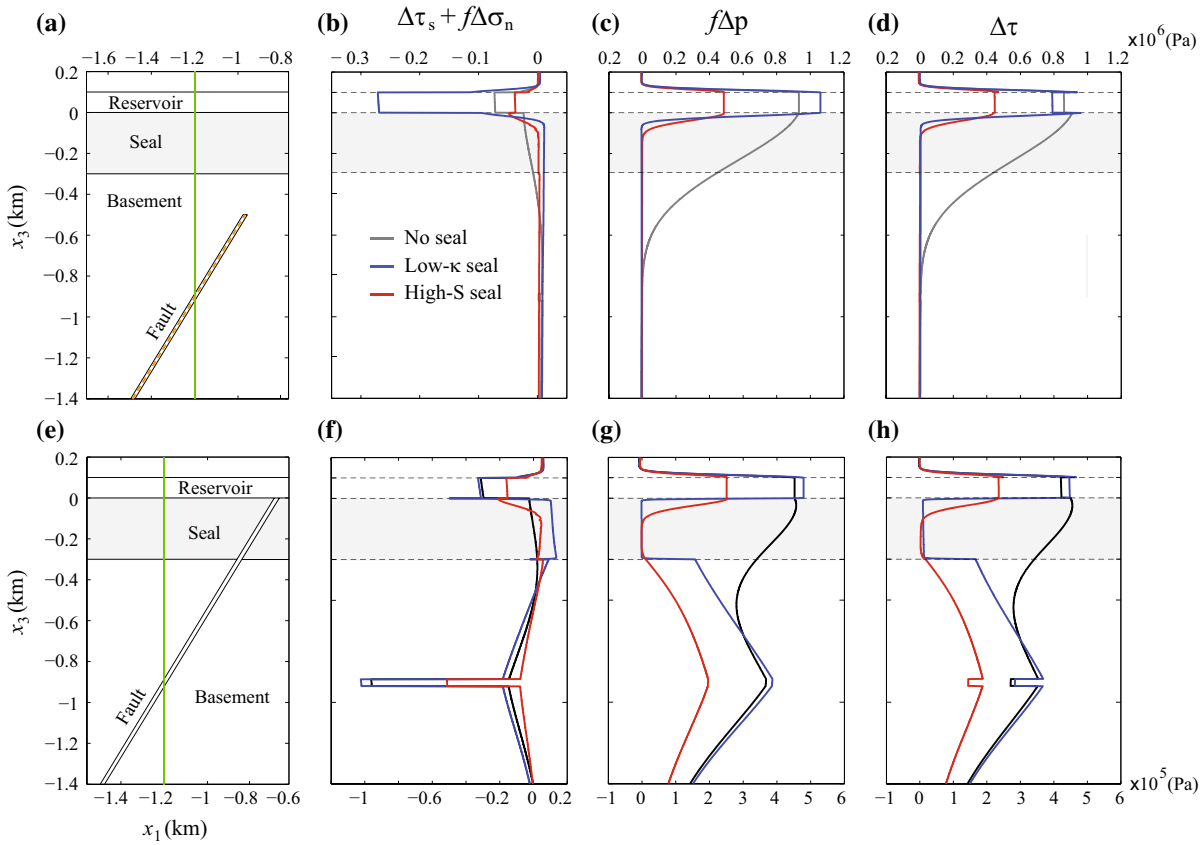

Figure 5
Vertical distribution of poroelastic stresses $\Delta\tau_s + f\Delta\sigma_n$, pore-pressure $f\Delta p$, and Coulomb stress $\Delta\tau$ along a *solid green line*, shown in **a**, **e**, at 200 days for three cases: no seal (*black*), low-permeability seal (*blue*), and high-storativity seal (*red*). **b**–**d** The basement faults isolated from the reservoir while **f**–**h** are for the faults hydraulically connected to the reservoir

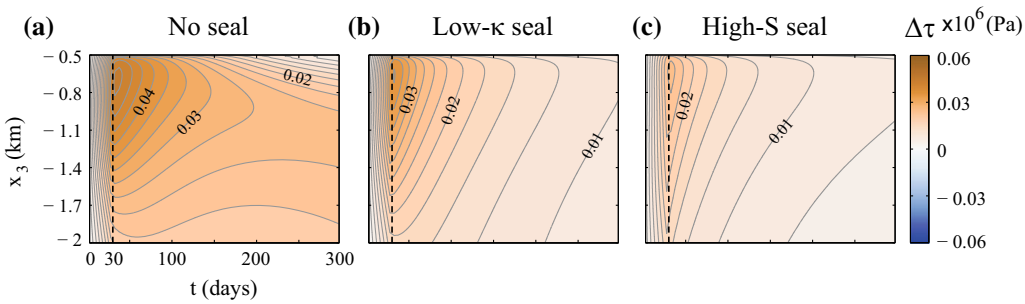

Figure 6
Temporal evolution of Coulomb stress change $\Delta\tau(t)$ in the *middle* of the fault nearest the injection well, indicated by a *dashed orange line* in Fig. 5a, for three cases. *Dashed lines on each plot* give the end of injection

seal reduce pore-pressure and poroelastic stresses in deep basement rocks (refer to Fig. 3), which reduces $\Delta\tau$ along the fault. Low-permeability seals inhibit pore-pressure diffusion into the basement, which may lessen the probability of fault failure (Fig. 6b). High-storativity bottom seals can absorb injection-induced pore-pressure increases and minimize the stress change, acting as a cushion, which for the chosen

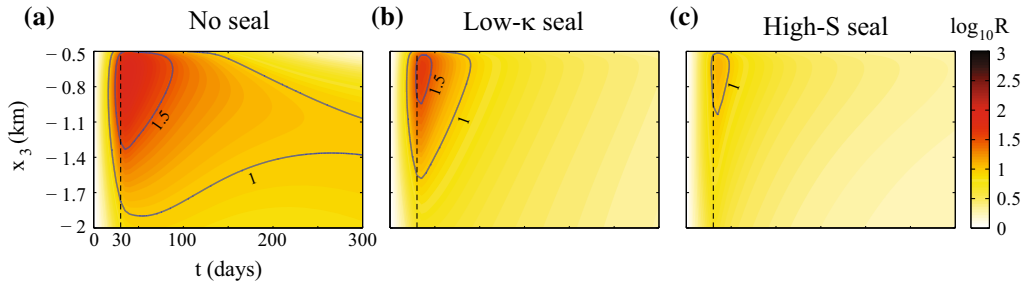

Figure 7
Seismicity rate $R(t)$ along the basement fault nearest the injection well, indicated by a *dashed orange line* in Fig. 5a, for three cases. *Dashed lines* indicate the end of well operations ($\Delta t = 30$ days)

parameters leads to even greater reduction in Coulomb stress (Fig. 6c).

3.3. Seismicity Rate Along Basement Faults

We have demonstrated that a low-permeability or high-storativity layer below the storage formation minimizes the diffusion of pore-pressure directly into the basement, which reduces the Coulomb stress change nearby basement faults. We next estimate the seismicity rate in the fault zone ($-2 < x_3 < -0.5$ km) using the seismicity rate model (12). Figure 7 shows the seismicity rate on a logarithmic scale, $\log_{10} R$, along the middle of the basement fault nearest the injection well, indicated as a dashed orange line in Fig. 5a. The vertical dashed line represents the end of injection ($\Delta t = 30$ days).

Without a bottom-sealing layer (Fig. 7a), poroelastic extension in the basement induces early seismicity, and post shut-in diffusion of pore-pressure causes later seismicity along the fault. In the case of a low-permeability seal, direct pore-pressure diffusion into the basement is reduced, lowering the seismicity rate at later times, but poroelastic stress is still transmitted to the basement faults (refer to Fig. 3b), resulting in an increase in the seismicity rate at early times (Fig. 7b). The high-storativity seal absorbs much of the direct pore-pressure diffusion from the target formation (refer to Fig. 3c), which reduces the seismicity rate significantly (Fig. 7c). The compressible sealing layer enhances storage capacity, minimizing the change in Coulomb stress and potentially the seismicity rate on basement faults. For both cases with a bottom seal, a lower seismicity rate is predicted due to smaller perturbation in Coulomb stress acting on the faults. This implies that a reservoir with bottom seals will be a better candidate formation to store large amounts of fluids, while minimizing potential earthquakes on basement faults.

4. Summary and Conclusion

This study has shown that a sealing layer beneath the target reservoir minimizes the potential of induced earthquakes on faults located in the basement. As in previous studies (Chang and Segall 2016a, b), we model full poroelastic coupling to understand the physical mechanisms behind injection-induced earthquakes in basement rocks including both direct pore-pressure changes along conductive basement faults as well as indirect perturbations in the stress state due to poroelastic effects. Our poroelastic calculations confirm that stress fields can be perturbed even at distances beyond the direct effect of pore-pressure change, i.e. the deep basement.

Here we examine how different types of basal seals affect the spatio-temporal distribution of pore-pressure and stresses acting on the basement faults. We have considered two types of underlying seals in this study: (1) low-permeability and (2) high-storativity seals. The low-permeability seal acts as a hydraulic barrier that reduces pore-pressure diffusion into the basement, such that direct pore-pressure effects of fluid injection on induced earthquakes are reduced. However, expansion of the storage

formation modifies both shear and total normal stresses, an effect that can extend into formations below the seal. The high-storativity bottom seal mitigates stresses acting on basement faults by absorbing injection-induced pore-pressure so that the indirect effect of changes in solid stress due to poroelastic deformation is also minimized.

Our results suggest that bottom seals with low permeability and high storativity can reduce significantly the potential of induced earthquakes in the basement. Therefore, the characterization of the physical properties of bounding sequences is important in evaluating the capacity for safe and efficient fluid injection in light of induced seismicity. The attenuation of injection-induced pore-pressure and stress changes into the underlying seal should be considered in studies of induced seismicity associated with geological fluid injection that aim to determine the failure potential of the basement faults.

Acknowledgements

This work was supported by the Stanford Center for Induced and Triggered Seismicity (SCITS). No data were used in producing this manuscript. We thank the reviewers and editor for helpful comments.

References

Anderson, G., & Johnson, H. (1999). A new statistical test for static stress triggering: Application to the 1987 Superstition Hills earthquake sequence. *Journal of Geophysical Research*, *104*, 20153–20168. doi:10.1029/1999JB900200.

Biot, M. A. (1941). General theory of three-dimensional consolidation. *Journal of Applied Physics*, *12*, 155–164.

Birkholzer, J. T., Zhou, Q., & Tsang, C. F. (2009). Large-scale impact of CO_2 storage in deep saline aquifer: a sensitivity study on pressure response in stratified systems. *International Journal of Greenhouse Gas Control*, *3*(2), 181–194.

Chang, K. W., & Segall, P. (2016a). Injection induced seismicity on basement faults including poroelastic stressing. *Journal of Geophysical Research: Solid Earth*, *121*(4), 2708–2726. doi:10.1002/2015JB012561.

Chang, K. W., & Segall, P. (2016b). Seismicity on basement faults induced by simultaneous fluid injection-extraction. *Pure and Applied Geophysics*, *173*(8), 2621–2636. doi:10.1007/s00024-016-1319-7.

Chang, K. W., Hesse, M. A., & Nicot, J. P. (2013). Reduction of lateral pressure propagation due to dissipation into ambient mudrocks during geological carbon dioxide storage. *Water Resources Research*, *49*, 2573–2588. doi:10.1002/wrcr.20197.

COMSOL Multiphysics (2014). COMSOL multiphysics user's guide. Burlington: COMSOL AB

Dieterich, J. H. (1994). A constitutive law for rate of earthquake production and its application to earthquake clustering. *Journal of Geophysical Research: Solid Earth*, *99*(B2), 2601–2618. doi:10.1029/93JB02581.

Dreij, K., Chaudhry, Q. A., Jernstrom, B., Morgenstern, R., & Hanke, M. (2011). A method for efficient calculation of diffusion and reactions of lipophilic compounds in complex cell geometry. *PLoS One*, *6*(8), 1–18.

Ellsworth, W. L. (2013). Injection-induced earthquakes. *Science*, *341*(6142), 1225942. doi:10.1126/science.1225942.

Frohlich, C., Ellsworth, W., Brown, W. A., Brunt, M., Luetgert, J., MacDonald, T., et al. (2014). The 17 May 2012M4.8 earthquake near Timpson, East Texas: An event possibly triggered by fluid injection. *Journal of Geophysical Research: Solid Earth*, *119*(1), 581–593. doi:10.1002/2013JB010755.

Ge, S., & Garven, G. (1992). Hydromechanical modeling of tectonically driven groundwater flow with application to the Arkoma Foreland Basin. *Journal of Geophysical Research*, *97*(B6), 9119–9144. doi:10.1029/92JB00677.

Ge, S., Liu, M., Lu, N., Godt, J. W., & Luo, G. (2009). Did the Zipingpu reservoir trigger the 2008 Wenchuan earthquake? *Geophysical Research Letters*, *36*(20), L20315. doi:10.1029/2009GL040349.

Horton, S. (2012). Disposal of hydrofracking waste water fluid by injection into subsurface aquifers triggers earthquake swarm in Central Arkansas with potential for damaging earthquake. *Seismological Society of America*, *83*(2), 250–260. doi:10.1785/gssrl.83.2.250.

Hou, Z., Rockhold, M. L., & Murray, C. J. (2012). Evaluating the impact of caprock and reservoir properties on potential risk of CO_2 leakage after injection. *Environmental Earth Sciences*, *66*(8), 2403–2415. doi:10.1007/s12665-011-1465-2.

Hughes, T. J. R. (2000). *The finite element method: Linear static and dynamic finite element analysis*. Mineola: Courier Dover Publ.

Islam, Md A, & Skalle, P. (2013). An experimental investigation of shale mechanical properties through drained and undrained test mechanisms. *Rock Mechanics and Rock Engineering*, *6*, 1391–1413. doi:10.1007/s00603-013-0377-8.

Kerenan, K. M., Savage, H. M., Abers, G. A., & Cochran, E. S. (2013). Potentially induced earthquakes in Oklahoma, USA: Links between wastewater injection and the 2011 M_w 5.7 earthquake sequence. *Geology*, *41*, 699–702. doi:10.1130/G34045.1.

Kerenan, K. M., Weingarten, M., Abers, G. A., Bekins, B. A., & Ge, S. (2014). Sharp increase in central Oklahoma seismicity since 2008 induced by massive wastewater injection. *Science*, *345*, 448. doi:10.1126/science.1255802.

Kim, S., & Hosseini, S. (2013). Above-zone pressure monitoring and geomechanical analyses for a field-scale CO_2 injection project, cranfield, ms. *Greenhouse Gases: Science and Technology*, *4*, 81–98. doi:10.1002/ghg.1388.

Kim, W. Y. (2013). Induced seismicity associated with fluid injection into a deep well in Youngstown, Ohio. *Journal of Geophysical Research*, *118*(7), 3506–3518. doi:10.1002/jgrb.50247.

Little, M. G., & Jackson, R. B. (2010). Potential impacts of leakage from deep CO_2 geosequestration on overlying freshwater aquifers. *Environmental Science & Technology*, *44*(23), 9225–9232. doi:10.1021/es102235w.

McGarr, A. (2014). Maximum magnitude earthquakes induced by fluid injection. *Journal of Geophysical Research*, *119*(2), 1008–1019. doi:10.1002/2013JB010597.

Neuzil, C. E. (1994). How permeable are clays and shale? *Water Resources Research*, *30*(2), 145–150. doi:10.1029/93WR02930.

Oppenheimer, D. H., Reasenberg, P. A., & Simpson, R. W. (1988). Fault plane solutions for the 1984 Morgan Hill, California earthquake sequence: Evidence for the state of stress on the Calaveras fault. *Journal of Geophysical Research*, *93*, 9007–9026. doi:10.1029/JB093iB08p09007.

Rice, J. R., & Cleary, M. P. (1976). Some basic stress diffusion solutions for fluid-saturated porous media with compressible constituents. *Reviews of Geophysics*, *14*, 227–241. doi:10.1029/RG014i002p00227.

Rieke, H. H., & Chilingarian, G. V. (1974). Compaction of argillaceous sediments. *Development in sedimentology* (Vol. 16). Amsterdam: Elsevier.

Segall, P. (2010). *Earthquake and volcano deformation*. Princeton: Princeton University Press.

Segall, P., & Lu, S. (2015). Injection induced seismicity: Poroelastic and earthquake nucleation effects. *Journal of Geophysical Research: Solid Earth*, *120*(7), 5082–5103. doi:10.1002/2015JB012060.

Shapiro, S. A., Dinske, C., & Langenbruch, C. (2010). Seismogenic index and magnitude probability of earthquakes induced during reservoir fluid stimulations. *The Leading Edge*, *29*(3), 304–309. doi:10.1190/1.3353727.

Siirila, E. R., Navarre-Sitchler, A. K., Maxwell, R. M., & McCray, J. E. (2012). A quantitative methodology to assess the risks to human health from CO2 leakage into groundwater. *Advances in Water Resources*, *36*, 146–164. doi:10.1016/j.advwatres.2010.11.005.

Song, J., & Zhang, D. (2013). Comprehensive review of caprock-sealing mechanisms for geologic carbon sequestration. *Environmental Science & Technology*, *47*(1), 9–22. doi:10.1021/es301610p.

Stanislavsky, E., & Garven, G. (2002). The minimum depth of fault failure in compressional environments. *Geophysical Research Letters*, *29*(24), 2155. doi:10.1029/2002GL016363.

Stein, R. S., & Lisowski, M. (1983). The 1979 Homestead Valley earthquake sequence, California: Control of aftershocks and postseismic deformation. *Journal of Geophysical Research*, *88*, 6477–6490. doi:10.1029/JB088iB08p06477.

Toda, S., Stein, R. S., Reasonberg, P. A., Dieterich, J. H., & Yoshida, A. (1998). Stress transferred by the 1995 Mw = 6.9 Kobe, Japan, shock. *Journal of Geophysical Research*, *103*, 24543–24565. doi:10.1029/98JB00765.

Tofflemire, T. J., & Brezner, G. P. (1971). Deep-well injection of wastewater. *Water Pollution Control Federation*, *43*(7), 1468–1479.

Vilarrasa, V., & Carrera, J. (2015). Geologic carbon storage is unlikely to trigger large earthquakes and reactivate faults through which CO_2 could leak. *Proceedings of the National Academy of Sciences*, *112*(19), 5938–5943. doi:10.1073/pnas.1413284112.

Walsh, F. R., & Zoback, M. D. (2015). Oklahoma's recent earthquakes and saltwater disposal. *Science Advances*, *1*(5), e1500195. doi:10.1126/sciadv.1500195.

Wang, H. F. (2000). *Theory of Linear Poroelasticity*. Princeton: Princeton University Press.

Willson, J. P., Lunn, R. J., & Shipton, Z. K. (2007). Simulating spatial and temporal evolution of multiple wing cracks around faults in crystalline basement rocks. *Journal of Geophysical Research*, *112*, B08408. doi:10.1029/2006JB004815.

Zhang, Y., Person, M., Rupp, J., Elett, K., Celia, M. A., Gable, C. W., et al. (2013). Hydrogeologic controls on induced seismicity in crystalline basement rocks due to fluid injection into basal reservoirs. *Ground Water*, *51*(4), 525–538. doi:10.1111/gwat.12071.

(Received September 6, 2016, revised May 2, 2017, accepted May 3, 2017)